Stabilization of highly efficient perovskite solar cells with a tailored supramolecular interface

Zhao, Chenxu; Zhou, Zhiwen; Almalki, Masaud; Zhao, Jiashang; Gallet, Thibaut; Savenije, Tom J.; Yao, Jianxi; Zhang, Hong; Grätzel, Michael; More Authors

DOI
10.1038/s41467-024-51550-z

Publication date
2024

Document Version
Final published version

Published in
Nature Communications

nature communications

Article

https://doi.org/10.1038/s41467-024-51550-z

Stabilization of highly efficient perovskite solar cells with a tailored supramolecular interface

Received: 4 March 2024

Accepted: 12 August 2024

Published online: 20 August 2024

Check for updates

Chenxu Zhao[1,2,3,10], Zhiwen Zhou[1,4,10] ✉, Masaud Almalki[1,5,10], Michael A. Hope[6], Jiashang Zhao[7], Thibaut Gallet[8], Anurag Krishna[1], Aditya Mishra[6], Felix T. Eickemeyer[1], Jia Xu[2], Yingguo Yang[9], Shaik M. Zakeeruddin[1], Alex Redinger[8], Tom J. Savenije[7], Lyndon Emsley[6], Jianxi Yao[2] ✉, Hong Zhang[3] ✉ & Michael Grätzel[1] ✉

The presence of defects at the interface between the perovskite film and the carrier transport layer poses significant challenges to the performance and stability of perovskite solar cells (PSCs). Addressing this issue, we introduce a dual host-guest (DHG) complexation strategy to modulate both the bulk and interfacial properties of $FAPbI_3$-rich PSCs. Through NMR spectroscopy, a synergistic effect of the dual treatment is observed. Additionally, electro-optical characterizations demonstrate that the DHG strategy not only passivates defects but also enhances carrier extraction and transport. Remarkably, employing the DHG strategy yields PSCs with power conversion efficiencies (PCE) of 25.89% (certified at 25.53%). Furthermore, these DHG-modified PSCs exhibit enhanced operational stability, retaining over 96.6% of their initial PCE of 25.55% after 1050 hours of continuous operation under one-sun illumination, which was the highest initial value in the recently reported articles. This work establishes a promising pathway for stabilizing high-efficiency perovskite photovoltaics through supramolecular engineering, marking a significant advancement in the field.

Metal halide perovskites are poised to revolutionize next-generation photovoltaics (PVs), owing to their exceptional optoelectronic properties and compatibility with low-cost, large-scale fabrication methods[1–8]. Similar to organic solar cells[9–11] and dye-sensitized solar cells[12], perovskite solar cells (PSCs) have a shorter energy payback time (more than 4 times) and lower equivalent greenhouse gas emissions than state-of-art crystalline silicon (c-Si) solar cells (less than 2 times) over their lifecycle[13]. The leap forward in a short period of time in the power conversion efficiency (PCE) in PSCs is unprecedented, with PCEs emerging from 3.8%[3] in its first study to a current certified value of

[1]Laboratory of Photonics and Interfaces, École Polytechnique Fédérale de Lausanne, Lausanne, Switzerland. [2]State Key Laboratory of Alternate Electrical Power System with Renewable Energy Sources, Beijing Key Laboratory of Energy Safety and Clean Utilization, North China Electric Power University, Beijing, P. R. China. [3]State Key Laboratory of Photovoltaic Science and Technology, Shanghai Frontiers Science Research Base of Intelligent Optoelectronics and Perception, Institute of Optoelectronics, Fudan University, Shanghai, China. [4]Department of Electronic Engineering, The Chinese University of Hong Kong, Shatin, Hong Kong SAR, China. [5]Future Energy Technology Institute, King Abdulaziz City for Science and Technology (KACST), P.O. Box 6086 Riyadh, Saudi Arabia. [6]Laboratory of Magnetic Resonance, Institute of Chemical Sciences and Engineering, École Polytechnique Fédérale de Lausanne, Lausanne, Switzerland. [7]Department of Chemical Engineering, Delft University of Technology, Delft, The Netherlands. [8]Scanning Probe Microscopy Laboratory, Department of Physics and Materials Science, University of, Luxembourg, Luxembourg. [9]School of Microelectronics, Fudan University, Shanghai, P. R. China. [10]These authors contributed equally: Chenxu Zhao, Zhiwen Zhou, Masaud Almalki. ✉e-mail: zwzhou@connect.hku.hk; jianxiyao@ncepu.edu.cn; hzhangioe@fudan.edu.cn; michael.graetzel@epfl.ch

26.7% in single-junction PSCs, approaching the performance level of c-Si solar cells[14]. Given their low manufacturing costs and impressive device performance, PSCs have the potential to significantly reduce the levelized cost of electricity, thereby economically driving the global energy transition[15]. However, despite their promise, the commercialization of PSCs is impeded by their operational stability issue, caused mostly by the unstable perovskite interface with the carrier transport layers[16,17]. Although tremendous efforts have been applied to solve these problems, it is still challenging to match the lifetime of silicon cells when operating state-of-the-art PSCs (PCE > 25%) under sunlight illumination at elevated temperatures.

Currently, there is an ongoing global effort to mitigate the instability of the emerging PSCs, and many of these endeavors are focused on developing new compositions, processing methods, and passivation strategies[18–26]. In particular, tailoring supramolecular agents with different structures and properties to reduce the concentration of defects in perovskite materials has been demonstrated to be an effective approach for enhancing the photovoltaic performance of PSCs (Supplementary Table 1)[19,22,23,27–53]. Previous studies have revealed that nanoscale impurities (e.g., PbI_2) and defects located at the bulk and surface of perovskite films play a crucial role in driving the rapid degradation of PSCs under sunlight illumination[54–56]. We recently showed that infusion of cesium iodide (CsI) into perovskite films through a supramolecular approach based on host–guest complexation effectively stabilized the photoactive perovskite phase by suppressing PbI_2 impurities and non-photoactive perovskite phases[27]. Although the photovoltaic performance and operational stability significantly improved, the insulating crown ether host molecule used creates a charge transport (hole transfer) barrier between the perovskite and the hole transport layer (HTL)[57].

Herein, we report a dual host–guest (DHG) complexation strategy to modulate the electrical and optoelectronic properties of $FAPbI_3$-rich perovskites. Specifically, we sequentially treat the perovskite surface with a Cs–crown-ether complex and an organic ammonium salt. NMR spectroscopy demonstrates that the ammonium environment is modified by the crown ether. Electro-optical characterizations show that the DHG strategy not only passivates surface and bulk defects but also improves the carrier transport between the perovskite and the HTL. The DHG-treated perovskite films exhibit less non-radiative charge carrier recombination losses, indicating a lower defect density, and a significantly improved charge extraction from the perovskite film to the HTL. We observed an improvement of ~ 60 mV for the open-circuit voltage (V_{OC}) of the DHG-treated perovskite devices as compared to the control devices. As a result, the best-performing device yielded a high PCE of 25.89% (25.53% certified), accompanied by an enhancement in operational stability. The DHG-treated PSCs retain over 96.6% of their initial PCE of 25.55% after 1050 h continuous operation under one-sun illumination. This work provides a simple yet effective approach to fabricating perovskite photovoltaics with outstanding performance and operational stability.

Results and discussion

Supramolecular interface design and structural characterizations

Figure 1a shows the concept of the supramolecular interface design in this work. First, the perovskite layer is treated with a solution of an alkali metal salt and a crown ether (in this case dibenzo-21-crown-7 (DB21C7), Fig. 1b **left**), so that the alkali metal is infused into the perovskite film upon annealing. We have previously demonstrated that treatment with a Cs–crown-ether complex results in a gradient of Cs^+ doping into the bulk of the perovskite, which is better than the homogeneous-doping passivation effect[27]. Second, the modified perovskite film is treated with an organic ammonium salt such as phenylethylammonium iodide (PEAI, Fig. 1b **right**). For simplicity, the perovskite treated with only the Cs–crown-ether complex is denoted as host–guest (HG) treatment; the perovskite sequentially treated with Cs–crown-ether complex and an organic ammonium salt is denoted as dual host–guest (DHG) treatment.

In order to investigate the interaction between PEA^+ and DB21C7, solid-state NMR spectra were recorded since NMR is sensitive to the local atomic structure, without a requirement for long-range order[58]. NMR has previously been applied to address various structural identification for halide perovskite materials[59–61], including the mode of operation of surface passivating agents[57,62–64]. The room temperature $^1H \rightarrow {}^{13}C$ cross-polarization NMR spectrum of a 1:1 mixture of DB21C7 and PEAI prepared by ball-milling (Fig. 1c and Supplementary Table 2) exhibits significantly broader resonances compared to neat DB21C7 and PEAI; this indicates a distribution of environments in the mixture arising from PEA^+–ether interactions and a reduction in crystallinity. In particular, the distinct ethylene oxide signals in DB21C7 around 70 ppm can no longer be discerned, instead a single broad resonance is observed. The complexation of PEA^+ is most clearly evidenced by a downfield shift of the aliphatic signals, from 35.2 and 44.4 ppm in PEAI to 33.6 and 43.4 ppm in the mixture (see dashed lines, Fig. 1c).

To determine the environments of DB21C7 and PEA^+ in treated perovskite samples, scraped thin films of $FAPbI_3$ with either HG or DHG treatments were studied. Here the concentrations of the species of interest are very low, therefore the experiments were performed at 100 K to improve sensitivity. The ^{13}C spectra of the neat modulators and their mixture show the same general features at 100 K as at room temperature (Fig. 1d and Supplementary Table 2), namely a broadening of the resonances and a shift of the PEA^+ aliphatic signals. The interaction of DB21C7 with the perovskite and/or PEA^+ in both $FAPbI_3$ samples is implied by the broad ^{13}C resonances, in particular the major ~ 70 ppm signal (Fig. 1d). Although the methylammonium signal at ~ 31 ppm obscures one of the aliphatic PEA^+ signals, the 42.8 ppm signal for DHG treated $FAPbI_3$ matches the shift of PEA^+ in the 1:1 DB21C7:PEAI mixture, rather than that of pure PEAI at 44.4 ppm. This is evidence that PEA^+ is complexed by DB21C7 following DHG treatment. We note that on the formation of a layered perovskite, e.g., $(PEA)_2PbI_4$, this aliphatic PEA^+ signal is observed at 44.7 ppm, ruling out the formation of a layered perovskite following DHG treatment[65]. This is further corroborated by grazing-incidence X-ray diffraction (GIXRD) results (Supplementary Fig. 1), which reveal only the presence of a PEAI layer and no formation of 2D perovskite PEA_2PbI_4 on 3D perovskite films following DHG treatment[66]. In summary, the NMR result shows that the crown ether modifies the environment of the ammonium salt in the dual treatment, indicating a cooperative supramolecular effect.

Furthermore, we employed X-ray diffraction to probe the crystallinity and structural properties of the control, HG-treated, and DHG-treated perovskite films, as shown in Supplementary Fig. 2. All films possess a well-crystallized photoactive α-phase of the 3D perovskite, indicating a good crystallinity for all films. Meanwhile, the crystallinity for HG and DHG films was also enhanced, probably because of the secondary crystal growth (SCG)[67,68] involved here during the post-annealing, leading to the increased diffraction intensity. A slight increase in the angle of the (100) reflections was also observed for the HG and DHG perovskite films, showing a slight decrease in lattice constant, ascribed to a low level of doping by Cs^+ cations with a smaller radius than the FA^+ cations.

Surface morphology and electronic properties

The surface morphology of the perovskite films was analyzed by scanning electron microscope (SEM). As shown in Supplementary Fig. 3, all perovskite films possess uniform morphology and similar compact textures with grain sizes of several hundred nanometers without observable pinholes. Meanwhile, the HG and DHG perovskite films show a slightly larger grain domain size than the control film, which tends to reduce grain boundaries and defects. The enlarged grain domain size for the HG and DHG films could be attributed to the

https://doi.org/10.1038/s41467-024-51550-z

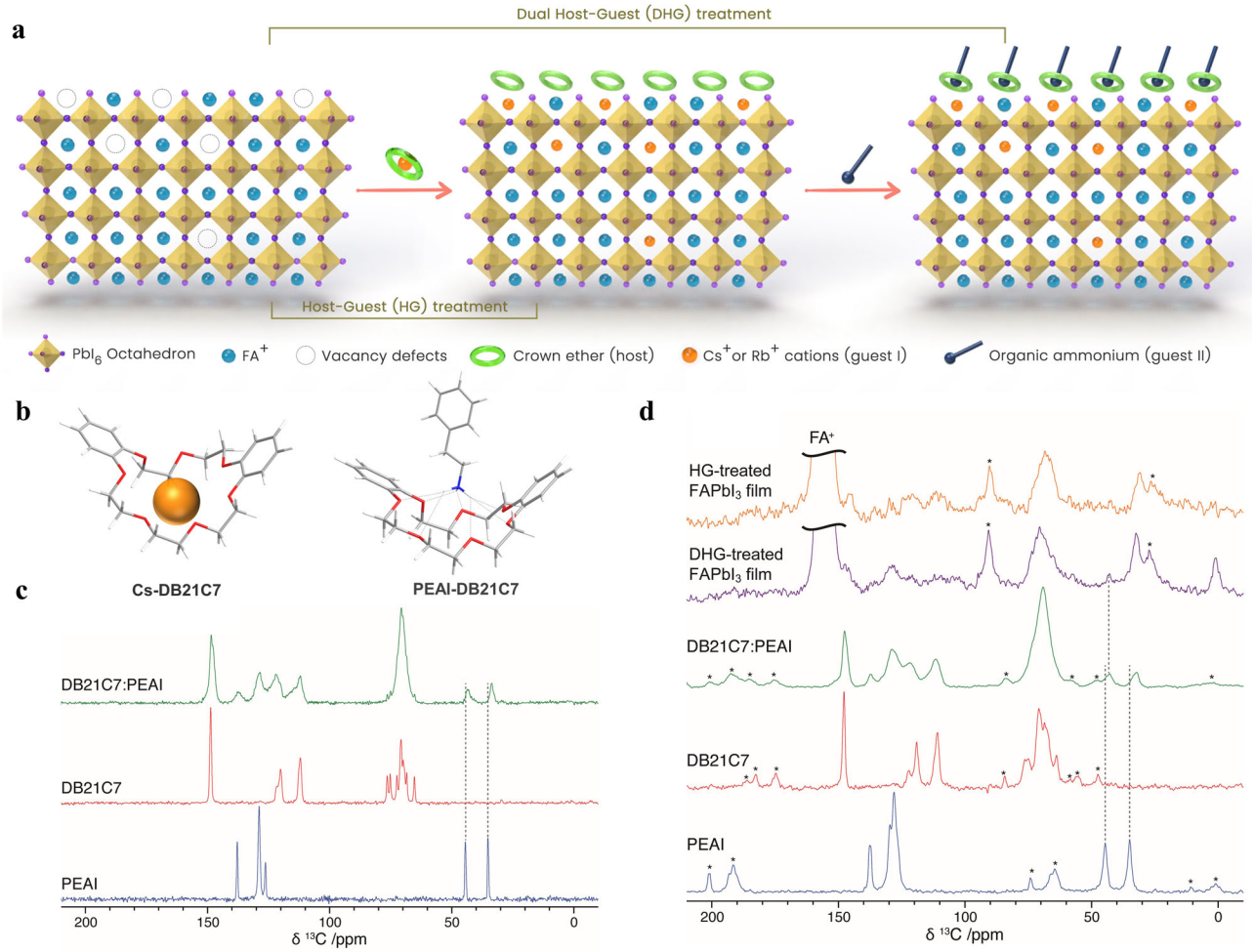

Fig. 1 | Supramolecular interface design and characterizations. a Schematic illustration of the supramolecular perovskite interface design. **b** The spatial interaction between the host molecule (DB21C7) with guest I (Cs^+, left) or guest II (PEA^+, right). **c**, **d** $^1H \rightarrow {}^{13}C$ NMR spectra of PEAI, DB21C7, and a ball-milled 1:1 mixture of the two, as well as scraped thin films of $FAPbI_3$ with HG treatment, or DHG treatment. **c** Spectra recorded at room temperature and 22 kHz MAS, and (**d**) spectra recorded at 100 K and 8 kHz MAS. The large FA^+ signal has been truncated, asterisks indicate spinning sidebands, and vertical lines are guides to the eye showing the change in shift of the PEA^+ aliphatic signals.

SCG, regarded as an essential means to achieve larger domain sizes and better crystallinity[67–70]. Having established the molecular-level interactions between the crown ether, PEAI, and perovskite layers in the target material, we next carried out a detailed surface analysis of grain boundaries (GBs) and grain interior/surface. Kelvin probe force microscopy (KPFM) measurements in an ultra-high vacuum (UHV) were recorded on the three types of samples, namely control, HG-treated, and DHG-treated perovskite films. Both post-treatments of the control sample led to the formation of smaller grains or precipitates on the surface (Fig. 2a and Supplementary Fig. 4). Interestingly, these smaller features were characterized by a much lower work function (*WF*) with respect to the rest of the surface, as depicted by the dotted red circles in the *WF* maps (Fig. 2b). Compared to the control sample, the *WF* of perovskite films were 160 and 200 meV lower on average after the HG and DHG treatments, respectively. These features could also be discerned in the broader distribution of the *WF* of the treated samples in Supplementary Fig. 4c. Most likely, these features were the result of an alkali metal-containing secondary phase[56]. Besides these low *WF* regions, the surface looked rather homogeneous, with some grain-to-grain variations, as previously observed in other reports[44,71,72]. The post-treatment also reduced the average *WF*, which decreased from 4.28 eV to 3.96 eV after the HG treatment and to 3.82 eV after the DHG treatment. This suggests that both treatments either changed the surface dipole or influenced the surface band bending. The decrease of the *WF* by such an amplitude improves both the hole extraction and the electron repelling at the perovskite/HTL interface[44,73]. In addition, a clear contrast was observed at the grain boundaries (GBs) for all samples, which often indicates an accumulation or depletion of charge at the GBs. Therefore, the GB band bending (*WF* difference between the grains and adjacent GB) was measured. The statistical analysis for each sample (more than a hundred grains investigated from several images) is depicted in Fig. 2c. For the control sample, the GB band bending (BB) was distributed equally, with 50% upward BB and 50% of downward BB. While the upward BB was not detrimental here, the downward BB of 100 meV could produce an accumulation of electrons at the GB and induce recombination as they are potential recombination centers[74,75]. The HG treatment reduced both the amount of downward BB (40%) and its magnitude to 40 meV, which is likely to be negligible as relatively close to *kT*. The DHG treatment further reduced the downward BB to 10%. This analysis shows that both surface treatments suppressed the possibility for electrons to recombine at the GBs and enhanced the hole extraction at the interface perovskite/HTM.

Next, scanning tunneling spectroscopy measurements were carried out to determine the surface bandgap and the local density of surface states (LDOS) at the surface[71]. Constant current imaging spectroscopy (CITS) maps were acquired in Supplementary Fig. 4b with their topography (Supplementary Fig. 4a) and used to extract the (dI/dV)/(), which is a better estimate of the LDOS and the surface

https://doi.org/10.1038/s41467-024-51550-z

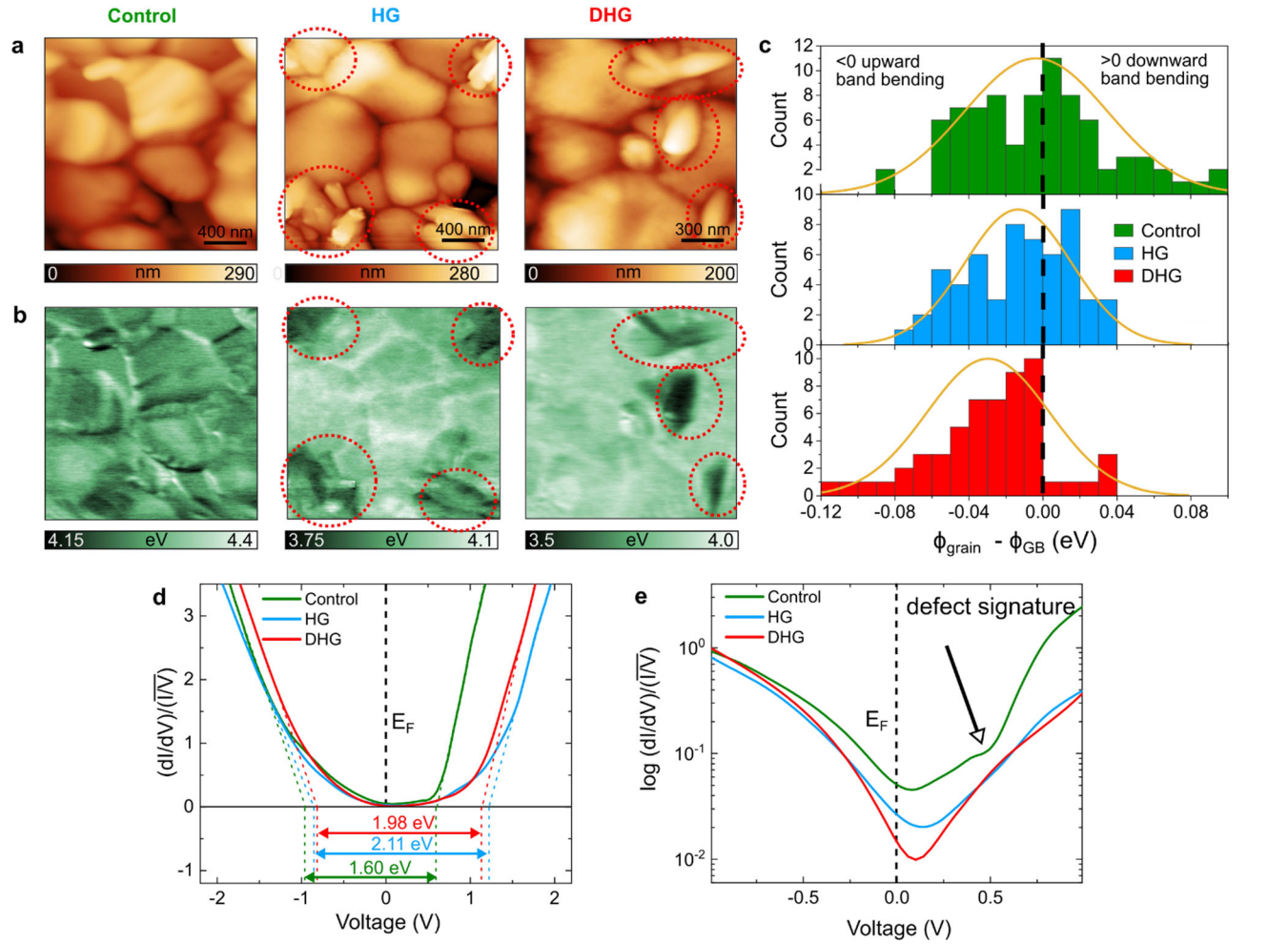

Fig. 2 | Surface morphology, potential, and the local density of states. a AFM topography of the control film and those with HG or DHG treatments. **b** Work function (WF) maps of (**a**). The red dotted circles represent precipitations occurring after the different treatments of the control sample. **c** Grain boundary band bending of all samples (work function difference between grains and grain boundaries). **d** Average scanning tunneling spectroscopy curves of the samples. A linear extrapolation (dotted lines) of the normalized and broadened LDOS curves was used to estimate the surface bandgap. **e** LDOS plotted on a log scale, exhibiting a defect signature for the control sample, which is suppressed on the other samples.

bandgap than the commonly used dI/dV[71,76]. The average curves are depicted in Fig. 2d, e with linear and logarithmic scales, respectively. The surface bandgap of the control sample was extrapolated to a 1.6 ± 0.05 eV value, which is a little bit larger than the bulk bandgap of the perovskite absorber. Compared with conventional semiconductors, perovskites have soft and flexible structures[77–79] and can exhibit lattice distortions such as octahedral tilting[80,81] and the atom off-centering[82–86], which is even more severe at the grain boundaries and interfaces. The lattice distortions at the top interface will inevitably widen the surface bandgap of the control sample. Furthermore, the surface bandgap increased to 2.1 ± 0.05 eV and to 2.0 ± 0.05 eV with the HG and DHG treatment, respectively, mainly due to the organic molecule existing on the top surface of the HG and DHG films. Multiple cooperative supramolecular interactions, including metal-organic coordination and hydrogen bonding, are realized by crown ether molecules spontaneously anchoring onto perovskite surfaces[87]. The supramolecular interactions lead to the formation of PbI_2-DB21C7 and PbI_2-DB21C7-PEAI complexes at the surface of the perovskite bulk, which will result in a further increase in surface bandgaps of HG- and DHG-treated samples. The crown ether and or the PEAI organic molecules could increase the superficial surface bandgap, which can suppress interfacial recombination at the perovskite/HTM interface.

Interestingly, we observed an increased tunneling conductance at positive applied voltages for the control sample, which was conspicuously absent in the HG and DHG samples. The removal of a defect state at the interface to the extraction layer reduces the surface recombination velocity and thereby improves V_{OC}, that have been discussed previously in the work of Anurag et al.[44]. The downshift of the tunneling conductance near E_F (0 V, Fig. 2e) after each treatment is consistent with the reduction of the *WF* observed via KPFM. Lastly, while the HG treatment mostly changed the LDOS at positive voltages (conduction band), the DHG treatment also shifted the LDOS at negative voltages (valence band). Both treatments, however, led to a more intrinsically doped surface compared to the control's surface, which was weakly n-doped (either the consequence of the bulk doping or a defect-induced surface band bending). The complementary KPFM and STS measurements, therefore, demonstrated that both surface treatments removed surface defects and increased the surface bandgap, thereby reducing non-radiative and interfacial recombination, decreasing the average *WF,* and suppressed the GB downward band bending, which otherwise promoted the electron recombination at the GBs. Ultimately, the DHG treatment proved to be more effective for most of these improvements.

https://doi.org/10.1038/s41467-024-51550-z

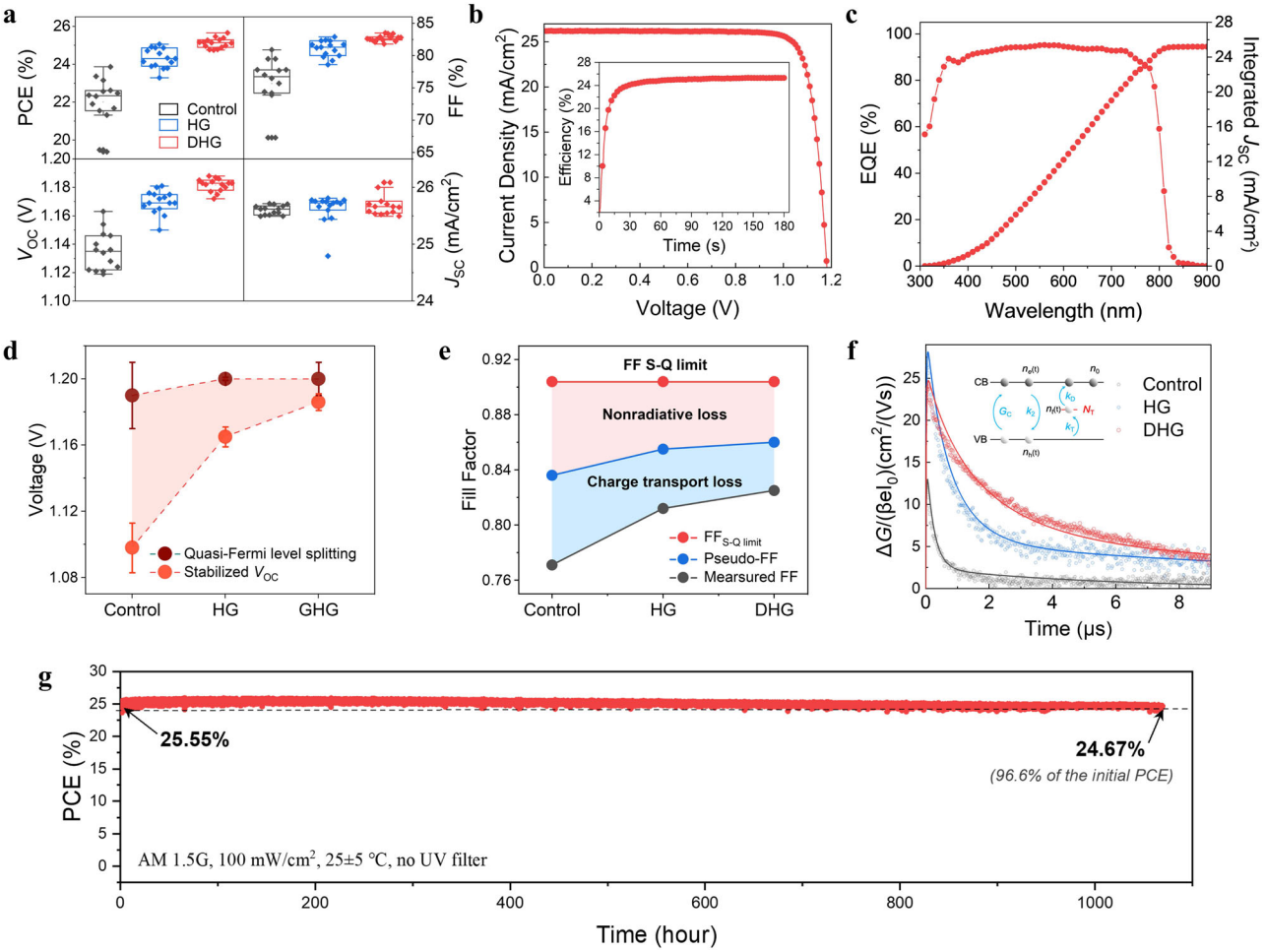

Fig. 3 | Devices performances and carrier dynamic characterizations. **a** Photovoltaic metrics of control, HG, and DHG-treated perovskite devices (based on 15 devices). PEAI was used as the guest-II molecule. **b** Best device performance based on DHG treatment. The inset shows the stabilized efficiency after maximum power point (MPP) tracking of the device for 180 s; OAI was used as the guest-II molecule. **c** EQE spectra (left axis) and integrated J_{SC} (right axis) for the champion DHG-treated PSCs. **d** Stabilized V_{OC} and quasi-Fermi level splitting $\Delta E_F/q$ for different perovskite films with spiro-OMeTAD deposited on glass (five individual samples were used per condition). **e** FF loss analysis of control, HG, and DHG devices. The device FF S-Q limit consists of charge-transport loss (blue area) and nonradiative loss (pink area). **f** Comparison of the time-resolved photoconductance traces for control, HG, and DHG-treated perovskite films recorded at an intensity of 5×10^9 photons cm^{-2} per pulse at 650 nm, corresponding to initial charge carrier densities of 5×10^{13} cm^{-3}. **g** Operational stability test for a high-efficiency DHG-treated PSC measured under full solar illumination (AM 1.5 G, 100 mW cm^{-2} under ambient conditions) at room temperature (25 ± 5 °C) without a UV filter.

Photovoltaic performance

To investigate the photovoltaic performance of the corresponding PSCs, a regular device structure was employed here, viz. FTO/compact layer (c-TiO_2)/mesoporous layer (m-TiO_2)/$(FAPbI_3)_{0.97}(MAPbBr_3)_{0.03}$ perovskite layer/hole transport layer (Spiro-OMeTAD)/Au. The statistical distribution of current density (J_{SC}), open-circuit voltage (V_{OC}), and fill factor (FF) determining the power-conversion efficiency (PCE) are shown in Fig. 3a. As expected from the defect concentration and carrier lifetime analysis of the perovskite thin films formed under each condition, the average PCE of the target device with DHG treatment was the highest, compared to the control and HG-treated devices. The improvement in the overall performance of the devices is mainly attributed to the improvement in the V_{OC} and the FF. The average V_{OC} was improved from 1.135 V (control) to 1.168 V (HG) and 1.183 V (DHG), while FF was improved from 77.1% (control) to 81.2% (HG) and 82.5% (DHG). Overall, the average PCE increased from 22.3% (control) to 24.4% (HG) and 25.3% (DHG). The corresponding *J-V* curves and parameters are illustrated in Supplementary Fig. 5 and Supplementary Table 3; the DHG-based device was almost hysteresis-free whereas the control device showed obvious hysteresis. It should be noted that both HG and DHG-treated PSCs show much higher performance than that of the device only treated with PEAI (Supplementary Fig. 6).

We further tested different organic ammonium salts (guest II) to investigate their photovoltaic performance (Supplementary Fig. 7), where the DHG treatment with n-octylammonium iodide shows the best performance. As shown in Fig. 3b, the champion device shows a PCE of 25.89% and a stabilized efficiency of 25.3%, which is the highest value for supramolecular-agent-modulated PSCs to the best of our knowledge (Supplementary Fig. 8). We validated the performance of our PSCs at the Photovoltaic and Wind Power Systems Quality Test Center, IEE, Chinese Academy of Sciences (PWQTC), and the certified parameters are shown in Supplementary Fig. 9. PCEs of 25.53% for reverse scan and 25.48% for forward scan were confirmed with negligible hysteresis. The external quantum efficiencies (EQEs) of the devices were measured (Fig. 3c) and the integrated currents match well with the J_{SC} values obtained from the *J-V* curves. We have expanded and employed the HG and DHG strategies in other perovskite systems, including narrow bandgap PSCs and wide bandgap PSCs (Supplementary Fig. 10 and Supplementary Tables 4, 5). The improvements in photovoltaic performance of the narrow bandgap PSCs and wide

bandgap PSCs treated with HG and DHG strategy confirmed their wide applicability.

The above results indicate that the interfacial non-radiative recombination process of the $FAPbI_3$-based perovskite films has been suppressed by supramolecular interface engineering. To further prove this, we determined the photoluminescence quantum yield (PLQY) and calculated quasi-Fermi level splitting (ΔE_F) according to the method described in Su et al.[57]. As shown in Supplementary Fig. 11, the PLQY of the device with DHG treatment is about 85 times higher than the control sample and 9 times higher than the HG samples. This indicates a significant decrease in the non-radiative recombination losses at the perovskite/HTL interface and grain boundaries, implying improved defect chemistry. From the PLQY, quasi-Fermi level splitting (ΔE_F) can be calculated with the following equation:

$$\Delta E_F = qV_{OC,rad} + kT\ln(PLQY) \quad (1)$$

where q is the elementary charge, $V_{OC,\,rad}$ is the radiative limit of V_{OC}, k is the Boltzmann constant, and T is the device temperature (25 °C)[88]. The internal voltage of the absorber ($\Delta E_F/q$), defined as the maximum V_{oc} that a solar cell can achieve if there are no additional losses present, is shown for the differently treated films in Fig. 3d. The control film shows a ΔE_F of 1.19 eV, and the target film with DHG treatment shows a ΔE_F of 1.2 meV. We measured the quasi-steady state V_{OC}, i.e., stabilized after two minutes of exposure under 1 sun-simulated illumination conditions. With DHG treatment, the V_{OC} increased by 76 mV from 1.096 V to 1.182 mV compared to the control sample, in good agreement with the trend seen in the ΔE_F measurements. The offsets between the stabilized V_{OC} and $\Delta E_F/q$ are 94 mV and 18 mV for the control and target devices, respectively, which can be explained by energetic misalignment at both interfaces as has been shown by Caprioglio et al.[89].

To investigate the influence of HG and DHG treatment on the device performance, in particular the device FF, we carried out intensity-dependent steady-state photoluminescence (PL) measurements and recorded external PLQYs for different perovskite films[90,91]. As shown in Supplementary Fig. 12, we plotted the calculated quasi-Fermi level splitting values (QFLSs) or implied V_{OC} (iV_{OC}) against the illumination intensity (Suns-V_{OC}) and then constructed pseudo-current density-voltage (pseudo-J–V) curves for control, HG, and DHG PSCs[92]. The pseudo-FF values calculated from the pseudo-J–V curves are 0.836, 0.855, and 0.864 for the control, HG, and DHG devices, respectively, and the FF loss analysis is summarized in Fig. 3e. The nonradiative loss for the HG and DHG devices was suppressed because interface defects were passivated by the HG and DHG strategies. Compared to the control device, the charge-transport loss in the HG and DHG devices, especially in the DHG device, was also clearly reduced owing to the increased carrier mobility, as shown above. These results confirmed that the DHG strategy not only inhibits non-radiative recombination but also improves charge transport in the device.

In order to further assess the impact of the supramolecular agent treatments on carrier transport and recombination, we performed time-resolved microwave conductivity (TRMC) measurements. This technique monitors the photoconductance (ΔG) on pulsed illumination, giving a direct measure of the mobile charge-carrier lifetimes, and mobilities as well as trap densities. Figure 3f shows the ΔG normalized by the number of incident photons as a function of time with photo-excitation at $\lambda = 650$ nm for the control and treated perovskite layers. The initial increase of the signal originates from the generation of free charge carriers, while the decay is attributed to recombination or to the immobilization of excess carriers by trapping. Several qualitative observations can be directly made: (1) Both treatments result in an increase in the charge carrier lifetime. (2) The TRMC signal size almost doubles with the HG treatment, while it decreases again slightly with the DHG treatment. (3) On increasing the laser intensity (Supplementary Fig. 13), the decay kinetics become faster, which can be explained by the fact that with higher initial charge densities the second-order band-to-band recombination leads to faster decay[93]. To obtain more quantitative data from these TRMC traces we fitted the time-resolved data using the kinetic model (see inset of Fig. 3f) previously used to describe the charge carrier dynamics[94,95]. The resulting rate constants and mobilities are collected in Supplementary Table 6. It is important to note here that all traces recorded at different intensities are described with one set of rate constants provided in the table. Without treatment, the mobility ($\Sigma\mu$) values amount to 26 $cm^2/(Vs)$ similar to previous values reported for FA-rich perovskites[96,97]. The $\Sigma\mu$ increases to 50 $cm^2/(Vs)$ with HG treatment and then reduces to 42 $cm^2/(Vs)$ for the DHG-treated sample. The large concentration of deep trap states (N_T) for the control layer leads to fast recombination almost independently of the laser intensity. Since the recombination occurs at the same time scale as the width of the laser pulse and the response time of the set-up, this leads to a relatively small maximum signal height. With the smaller value of N_T for the HG-treated perovskite layers, the charge carrier lifetime increases and results in a doubling of the initial height. Finally, for the DHG-treated sample we cannot assume that the sample is homogenous, and we need to include a thin surface layer in which holes can reside. Since the holes are partially collected in this surface layer, they are physically separated from the conduction band electrons leading to longer charge carrier lifetimes[98]. At the same time, the mobility values for those holes in the surface layer are substantially smaller. Both effects lead to the somewhat smaller signal height but slower decay kinetics as observed in Fig. 3f. These photo-conductance results confirm the effectively suppressed carrier recombination in perovskite films with a tailored supramolecular interface.

Finally, the operational stability of the DHG-treated PSCs was tested with maximum power point (MPP) tracking under sun illumination without a UV cutoff filter under ambient conditions. All the samples for the stability test were prepared by using spiro-OMeTAD materials as the hole transport layer. As shown in Fig. 3g, the unencapsulated DHG-treated device retained approximately 96.6% of its initial efficiency (25.55%) after 1050 h at room temperature (25 ± 5 °C), which was the highest initial value in the recently reported articles (Supplementary Table 7). After 500 h of full solar intensity light soaking under maximum power point tracking, the control, HG-treated, and DHG devices maintained 73.4%,94.5%, and 98.7% of their initial PCEs (Supplementary Fig. 14), respectively, showing that the DHG-treated PSC exhibited superior operational stability. What's more, the DHG-treated device also showed excellent operational stability at higher operating temperatures. When the temperature increased to 45 ± 5 °C, the unencapsulated DHG-treated device could maintain 88% of its initial efficiency (25.5%) after 500 h of continuous testing (Supplementary Fig. 15). To further test the thermal stability of the DHG-treated devices, the control and DHG treated PSCs were aged at 85 °C under an ambient condition with an RH (relative humidity) of 20%. As shown in Supplementary Fig. 16, the DHG-treated devices possess better thermal stability, since the PCE dropped by less than 20% after 600 h of thermal aging, while the PCEs of control samples decreased by around 40%. The superior ambient and operational stability can be attributed to the enhanced hydrophobicity and the decreased surface defect density in the perovskite absorber through supramolecular interface engineering.

Discussion

In conclusion, our study presents an innovative supramolecular modulation strategy aimed at fine-tuning the interface properties of $FAPbI_3$-rich based PSCs. Notably, the best-performing perovskite solar cells achieved an exceptional PCE of 25.89% (25.53% certified), alongside marked improvements in operational stability. The remarkable performance and stability of these devices can be attributed to the

synergistic supramolecular interactions between the passivating ammonium amphiphile and the crown ether at the critical interface between the perovskite layer and the hole conductor. This assertion is supported by detailed NMR analysis and further validated through comprehensive multiscale characterization, including examinations of local structure, grain/GB band-bending modulation, alterations in surface bandgap, LDOS, and interface defects. Our findings pave the way for a novel approach utilizing supramolecular chemistry with tailored non-covalent interactions for effective interfacial passivation in hybrid perovskite materials. This work holds significant promise for advancing the performance and stability of perovskite-based optoelectronic devices, thereby contributing to the broader landscape of sustainable energy technologies.

Methods

Materials

Lead iodide (PbI_2) was purchased from Alfa Aesar. Formamidinium iodide (FAI) and titanium dioxide paste (TiO_2 – 30 NRD) were purchased from Greatcell. 2,2′,7,7′-Tetrakis[N,N-di(4-methoxyphenyl) amino]−9,9′-spirobifluorene (Spiro-OMeTAD), n-Octylammonium Iodide (OAI), Phenethylamine Hydroiodid (PEAI), Benzylamine Hydroiodide (PMAI), 4-t-butylphenylmethylammonium Iodide (tBBAI), Fluorophenylethylammonium Iodide (FPEAI) were purchased from Xi'an Polymer Light Technology Corp. Methylammonium lead tribromide ($MAPbBr_3$) purchased from Share Chem. Ultra-dry dimethylformamide (DMF), dimethyl sulfoxide (DMSO), ethanol (EtOH), and chlorobenzene (CB) were purchased from Acros. Dibenzo-21-crown-7 (DB21C7), Cesium Iodide (CsI), 4-tert-butyl pyridine (TBP), lithium bis(trifluorosulfonyl) imide (Li-TFSI), acetonitrile (ACN), acetyl acetone, titanium diisopropoxide bis (acetylacetonate) 75 wt.% in isopropanol, and methylammonium chloride (MACl) were purchased from Sigma-Aldrich. Fluorine-doped tin oxide (FTO) (10 Ω/sq) conductive glass is purchased from Nippon Sheet Glass (NSG). All the chemicals were used as received without further purification.

Fabrication of perovskite films

Fluoride-doped tin oxide glass substrates (FTO, 4.0 mm-thick, 10 Ω/sq, Nippon Sheet Glass) were patterned using zinc powder and concentrated hydrochloric acid (1 M). The patterned FTO was sequentially cleaned with a 2 % commercial detergent (Hellmanex) water solution, deionized water, ethanol, and acetone in an ultrasonic bath for 15 min, rinsed with deionized water, and then dried by air blowgun. After O_3/ultraviolet treatment for 15 min, the 20–40 nm compact layer TiO_2 (c-TiO_2) was deposited on a cleaned FTO substrate by spray pyrolysis at 450 °C using a precursor solution of titanium diisopropoxide bis(acetylacetonate) with oxygen as the carrier gas. The precursor solution was prepared by taking 75 wt.% diisopropoxide bis(acetylacetonate) in isopropanol, diluting with ethanol with a volume ratio of 1:9, and addition of 4 vol% acetylacetone. After cooling down to room temperature and O_3/ultraviolet treatment for 15 min, the mesoporous TiO_2 (mp-TiO_2) was spin-coated at 4000 rpm for 20 s onto the c-TiO_2 using a commercial paste (Dyesol 30 NR-D) diluted in ethanol (1:6, weight ratio) to achieve 100 to 150 nm thickness. After drying at 80 °C for 10 min, the TiO_2 films were gradually sintered to 450 °C, kept at this temperature for 30 min, and cooled to room temperature. Before use, the films were treated with 0.1 M solution of Li-TFSI in acetonitrile by spin coating at 3000 rpm for 20 s and then were sintered at 450 °C for 30 min. After cooling down to 150 °C, the substrates were transferred to a dry-air glovebox (relative humidity < 15%) for deposition of perovskite films. The perovskite film was deposited onto the mp-TiO_2 substrate from a precursor solution containing lead iodide (1.51 M, Alfa Aesar), formamidinium iodide (1.47 M, Greatcell), and methylammonium bromide (0.03 M, Greatcell), lead bromide (0.03 M, TCI) and methylammonium chloride (0.6 M, Sigma-Aldrich) in anhydrous dimethylformamide (Acros)/ dimethylsulfoxide (Acros) (4:1 (v:v)) solution. The precursor solution was spin-coated in a two-step process at 1000 rpm for 10 s and 6000 rpm for 25 s, respectively. During the second step, 200–300 µL of chlorobenzene (Acros) was dropped on the spinning substrate 10 s prior to the end of the process. The substrates were sequentially heated at 150 °C for 10 min for perovskite crystal formation.

HG treatment

100 µL of the corresponding alkali metal crown ether complex (Cs-DB21C7) in chlorobenzene (CB) with various concentrations (5, 10, 15, 20 mM) were dynamically spin-coated on to the as-formed perovskite films at 4000 rpm for 20 s. The treated perovskite films were heated at 100 °C for 5 min, followed by CB washing.

DHG treatment

100 µL of the corresponding alkali metal crown ether complex (Cs-DB21C7) in chlorobenzene (CB) with various concentrations (5, 10, 15, 20 mM) were dynamically spin-coated on to the as-formed perovskite films at 4000 rpm for 20 s. The treated perovskite films were heated at 100 °C for 5 min, followed by CB washing. After that, organic ammonium salts in isopropanol (IPA) (2 mg/mL) were spin-coated onto perovskite films, followed by an annealing treatment at 50 °C for 5 min.

Fabrication of HTL and Au electrode

A hole transport material solution containing 75 mM spiro-OMeTAD (> 99.5%, Xi'an Polymer Light Technology Corp.) in chlorobenzene with 40 mM Li-TFSI (99.95%, Sigma-Aldrich) and 270 mM tBP (96%, Sigma-Aldrich) additives was dynamically spin-coated onto the substrate at 3000 rpm for 30 s. Finally, a gold electrode (~ 70 nm) with a size of 5 mm × 5 mm was deposited by thermal evaporation.

Photovoltaic performance measurement

The perovskite solar cells were measured using a 300 W Xenon light source from Oriel. The spectral mismatch between AM 1.5 G and the solar simulator was calibrated by a Schott K113 Tempax filter (Prazosopms G; as & Optik GmbH). A silicon photodiode was used as the light intensity calibrator for each measurement. A Keithley 2400 is used for the current-voltage scan by applying an external voltage bias and measuring the response current with a scan rate of 50 mV/s. An anti-reflection coating was used for the champion devices. The device area was 0.25 cm^2 (0.5 cm × 0.5 cm). The cells were masked with a black metal mask with a defined area of 0.16 cm^2.

Reporting summary

Further information on research design is available in the Nature Portfolio Reporting Summary linked to this article.

Data availability

The experiment data that support the findings of this study are available from the corresponding author upon reasonable request. The source data underlying Fig. 4a–e, and Supplementary Fig. 5a, as well as Supplementary Table 3, are provided as a Source Data file. Source data are provided in this paper.

References

1. Sha, W. E. I., Ren, X., Chen, L. & Choy, W. C. H. The efficiency limit of $CH_3NH_3PbI_3$ perovskite solar cells. *Appl. Phys. Lett.* **106**, 221104 (2015).
2. Liang, P.-W. et al. Additive enhanced crystallization of solution-processed perovskite for highly efficient planar-heterojunction solar cells. *Adv. Mater.* **26**, 3748–3754 (2014).
3. Kojima, A., Teshima, K., Shirai, Y. & Miyasaka, T. Organometal halide perovskites as visible-light sensitizers for photovoltaic cells. *J. Am. Chem. Soc.* **131**, 6050–6051 (2009).

4. Tan, H. et al. Efficient and stable solution-processed planar perovskite solar cells via contact passivation. *Science* **355**, 722–726 (2017).
5. Rong, Y. et al. Challenges for commercializing perovskite solar cells. *Science* **361**, eaat8235 (2018).
6. Lin, R. et al. All-perovskite tandem solar cells with 3D/3D bilayer perovskite heterojunction. *Nature* **620**, 994–1000 (2023).
7. Kim, H. J., Han, G. S. & Jung, H. S. Managing the lifecycle of perovskite solar cells: Addressing stability and environmental concerns from utilization to end-of-life. *eScience* **4**, 100243 (2024).
8. Zhu, A. et al. Playdough-like carbon electrode: A promising strategy for high efficiency perovskite solar cells and modules. *eScience* **4**, 100221 (2024).
9. Lu, J. et al. Non-covalent intramolecular interactions induced high-performance terpolymer donors. *Adv. Funct. Mater.* **34**, 2312545 (2024).
10. Yang, S. et al. Conformational locking control of 2D outer side chains via fluorine atom positioning for improving the thermal stability of organic solar cells. *ACS Appl. Mater. Interfaces* **15**, 39636–39646 (2023).
11. Zhong, L. et al. Solid additive delicately controls morphology formation and enables high-performance in organic solar cells. *Adv. Funct. Mater.* **33**, 2305450 (2023).
12. Ren, Y. et al. Hydroxamic acid pre-adsorption raises the efficiency of cosensitized solar cells. *Nature* **613**, 60–65 (2023).
13. Tian, X., Stranks, S. D. & You, F. Life cycle assessment of recycling strategies for perovskite photovoltaic modules. *Nat. Sustain.* **4**, 821–829 (2021).
14. Lin, H. et al. Silicon heterojunction solar cells with up to 26.81% efficiency achieved by electrically optimized nanocrystalline-silicon hole contact layers. *Nat. Energy* **8**, 789–799 (2023).
15. Li, Z. et al. Cost analysis of perovskite tandem photovoltaics. *Joule* **2**, 1559–1572 (2018).
16. Shao, S. & Loi, M. A. The role of the interfaces in perovskite solar cells. *Adv. Mater. Interfaces* **7**, 1901469 (2020).
17. Wang, Y. et al. Stabilizing heterostructures of soft perovskite semiconductors. *Science* **365**, 687–691 (2019).
18. Zhang, H., Pfeifer, L., Zakeeruddin, S. M., Chu, J. & Grätzel, M. Tailoring passivators for highly efficient and stable perovskite solar cells. *Nat. Rev. Chem.* **7**, 632–652 (2023).
19. Zhu, H. et al. Tailored amphiphilic molecular mitigators for stable perovskite solar cells with 23.5% efficiency. *Adv. Mater.* **32**, 1907757 (2020).
20. Zhang, Y. et al. Depth-dependent defect manipulation in perovskites for high-performance solar cells. *Energy Environ. Sci.* **14**, 6526–6535 (2021).
21. Zhu, P. et al. Simultaneous contact and grain-boundary passivation in planar perovskite solar cells using SnO_2-KCl composite electron transport layer. *Adv. Energy Mater.* **10**, 1903083 (2020).
22. Du, X. et al. Synergistic crystallization and passivation by a single molecular additive for high-performance Perovskite solar cells. *Adv. Mater.* **34**, 2204098 (2022).
23. Zhou, Q. et al. Multifunctional chemical bridge and defect passivation for highly efficient inverted perovskite solar cells. *ACS Energy Lett.* **6**, 1596–1606 (2021).
24. Tress, W. et al. Interpretation and evolution of open-circuit voltage, recombination, ideality factor and subgap defect states during reversible light-soaking and irreversible degradation of perovskite solar cells. *Energy Environ. Sci.* **11**, 151–165 (2018).
25. Zhao, T., Chueh, C.-C., Chen, Q., Rajagopal, A. & Jen, A. K. Y. Defect passivation of organic–inorganic hybrid perovskites by diammonium iodide toward high-performance photovoltaic devices. *ACS Energy Lett.* **1**, 757–763 (2016).
26. Wang, S. et al. Suppressed recombination for monolithic inorganic perovskite/silicon tandem solar cells with an approximate efficiency of 23%. *eScience* **2**, 339–346 (2022).
27. Zhang, H. et al. Multimodal host-guest complexation for efficient and stable perovskite photovoltaics. *Nat. Commun.* **12**, 3383 (2021).
28. Meng, Y. et al. Pre-buried ETL with bottom-Up strategy toward flexible perovskite solar cells with efficiency over 23%. *Adv. Funct. Mater.* **33**, 2214788 (2023).
29. Zhao, C. et al. Stabilization of $FAPbI_3$ with multifunctional alkali-functionalized polymer. *Adv. Mater.* **35**, 2211619 (2023).
30. Ruiz-Preciado, M. A. et al. Supramolecular modulation of hybrid perovskite solar cells via bifunctional halogen bonding revealed by two-dimensional 19Fsolid-state NMR spectroscopy. *J. Am. Chem. Soc.* **142**, 1645–1654 (2020).
31. Li, G. et al. Highly efficient p-i-n perovskite solar cells that endure temperature variations. *Science* **379**, 399–403 (2023).
32. Shen, Y. et al. Functional ionic liquid polymer stabilizer for high-performance perovskite photovoltaics. *Angew. Chem. Int. Ed.* **62**, e202300690 (2023).
33. Zhang, J. et al. Thermally crosslinked F-rich polymer to inhibit lead leakage for sustainable perovskite solar cells and modules. *Angew. Chem. Int. Ed.* **62**, e202305221 (2023).
34. Yang, M. F. et al. Reducing lead toxicity of perovskite solar cells with a built-in supramolecular complex. *Nat. Sustain.* **6**, 1455–1464 (2023).
35. Zhang, Y. et al. Improved fatigue behaviour of perovskite solar cells with an interfacial starch–polyiodide buffer layer. *Nat. Photonics* **17**, 1066–1073 (2023).
36. Wang, H. et al. Modulating buried interface with multi-fluorine containing organic molecule toward efficient NiO_x-based inverted perovskite solar cell. *Nano Energy* **111**, 108363 (2023).
37. Ru, P. et al. High electron affinity enables fast hole extraction for efficient, flexible, inverted perovskite solar cells. *Adv. Energy Mater.* **10**, 1903487 (2020).
38. Li, F. et al. Regulating surfacetermination for efficient innverted perovskite solar sells with greater than 23% efficiency. *J. Am. Chem. Soc.* **142**, 20134–20142 (2020).
39. Han, T. H. et al. Spontaneous hybrid cross-linked network induced by multifunctional copolymer toward mechanically resilient perovskite solar cells. *Adv. Funct. Mater.* **32**, 2207142 (2022).
40. Wang, K. et al. Defect passivation in perovskite solar cells by cyano-based π-conjugated molecules for improved performance and stability. *Adv. Funct. Mater.* **30**, 2002861 (2020).
41. Wang, M. H. et al. Rational selection of the polymeric structure for interface engineering of perovskite solar cells. *Joule* **6**, 1032–1048 (2022).
42. Zhang, B. et al. A multifunctional polymer as an interfacial layer for efficient and stable perovskite solar cells. *Angew. Chem. Int. Ed.* **62**, e202213478 (2023).
43. Fu, Q. et al. Multifunctional two-dimensional polymers for perovskite solar cells with efficiency exceeding 24%. *ACS Energy Lett.* **7**, 1128–1136 (2022).
44. Krishna, A. et al. Nanoscale interfacial engineering enables highly stable and efficient perovskite photovoltaics. *Energy Environ. Sci.* **14**, 5552–5562 (2021).
45. Kim, K. et al. Liquid-state dithiocarbonate-based polymeric additives with monodispersity rendering perovskite solar cells with exceptionally high certified photocurrent and fill factor. *Adv. Energy Mater.* **13**, 2203742 (2023).
46. Chen, Z. et al. Perovskite grain-boundary manipulation using room-temperature dynamic self-healing "ligaments" for developing highly stable flexible perovskite solar cells with 23.8% efficiency. *Adv. Mater.* **35**, 2300513 (2023).

47. Cao, Q. et al. Star-polymer multidentate-cross-linking strategy for superior operational stability of inverted perovskite solar cells at high efficiency. *Energy Environ. Sci.* **14**, 5406–5415 (2021).
48. Chen, N. L. et al. An efficient trap passivator for perovskite solar cells: poly(propylene glycol) bis(2-aminopropyl ether). *Nano Micro Lett.* **12**, 177 (2020).
49. Cao, Q. et al. Environmental-friendly polymer for efficient and stable inverted perovskite solar cells with mitigating lead leakage. *Adv. Funct. Mater.* **32**, 2201036 (2022).
50. Yu, B. et al. Application of a new π-conjugated ladder-like polymer in enhancing the stability and efficiency of perovskite solar cells. *J. Mater. Chem. A* **8**, 1417–1424 (2020).
51. Zhao, Y. P. et al. A polymerization-assisted grain growth strategy for efficient and stable perovskite solar cells. *Adv. Mater.* **32**, 1907769 (2020).
52. Li, M. et al. Orientated crystallization of FA-based perovskite via hydrogen-bonded polymer network for efficient and stable solar cells. *Nat. Commun.* **14**, 573 (2023).
53. Zhang, H. et al. Controllable heterogenous seeding-induced crystallization for high-efficiency $FAPbI_3$-based perovskite solar cells over 24%. *Adv. Mater.* **34**, 2204366 (2022).
54. Tennyson, E. M., Doherty, T. A. S. & Stranks, S. D. Heterogeneity at multiple length scales in halide perovskite semiconductors. *Nat. Rev. Mater.* **4**, 573–587 (2019).
55. Macpherson, S. et al. Local nanoscale phase impurities are degradation sites in halide perovskites. *Nature* **607**, 294–300 (2022).
56. Zhao, Y. et al. Inactive (PbI2)2RbCl stabilizes perovskite films for efficient solar cells. *Science* **377**, 531–534 (2022).
57. Su, T.-S. et al. Crown ether modulation enables over 23% efficient formamidinium-based perovskite solar cells. *J. Am. Chem. Soc.* **142**, 19980–19991 (2020).
58. Reif, B., Ashbrook, S. E., Emsley, L. & Hong, M. Solid-state NMR spectroscopy. *Nat. Rev. Methods Prim.* **1**, 2 (2021).
59. Piveteau, L., Morad, V. & Kovalenko, M. V. Solid-state NMR. and NQR. spectroscopy of lead-halide perovskite materials. *J. Am. Chem. Soc.* **142**, 19413–19437 (2020).
60. Franssen, W. M. J. & Kentgens, A. P. M. Solid–state NMR of hybrid halide perovskites. *Solid State Nucl. Magn. Reson.* **100**, 36–44 (2019).
61. Kubicki, D. J., Stranks, S. D., Grey, C. P. & Emsley, L. NMR spectroscopy probes microstructure, dynamics and doping of metal halide perovskites. *Nat. Rev. Chem.* **5**, 624–645 (2021).
62. Akhavan Kazemi, M. A. et al. Molecular-level insight into correlation between surface defects and stability of methylammonium lead halide perovskite under controlled humidity. *Small Methods* **5**, 2000834 (2021).
63. Alanazi, A. Q. et al. Atomic-level microstructure of efficient formamidinium-based perovskite solar cells stabilized by 5-ammonium valeric acid iodide revealed by multinuclear and two-dimensional solid-state NMR. *J. Am. Chem. Soc.* **141**, 17659–17669 (2019).
64. Mishra, A. et al. Dynamic nuclear polarization enables NMR of surface passivating agents on hybrid perovskite thin films. *J. Am. Chem. Soc.* **144**, 15175–15184 (2022).
65. Hope, M. A. et al. Nanoscale phase segregation in supramolecular π-templating for hybrid perovskite photovoltaics from NMR crystallography. *J. Am. Chem. Soc.* **143**, 1529–1538 (2021).
66. Jiang, Q. et al. Surface passivation of perovskite film for efficient solar cells. *Nat. Photonics* **13**, 460–466 (2019).
67. Li, Z. et al. Stabilizing perovskite structures by tuning tolerance factor: Formation of formamidinium and cesium lead iodide solid-state alloys. *Chem. Mater.* **28**, 284–292 (2016).
68. Liu, Z. et al. Grain regrowth and bifacial passivation for high-efficiency wide-bandgap perovskite solar cells. *Adv. Energy Mater.* **13**, 2203230 (2023).
69. Xie, F. X. et al. Vertical recrystallization for highly efficient and stable formamidinium-based inverted-structure perovskite solar cells. *Energy Environ. Sci.* **10**, 1942–1949 (2017).
70. Jin, Z. X. et al. Enhanced efficiency and stability in Sn-based perovskite solar cells with secondary crystallization growth. *J. Energy Chem.* **54**, 414–421 (2021).
71. Gallet, T., Grabowski, D., Kirchartz, T. & Redinger, A. Fermi-level pinning in methylammonium lead iodide perovskites. *Nanoscale* **11**, 16828–16836 (2019).
72. Leblebici, S. Y. et al. Facet-dependent photovoltaic efficiency variations in single grains of hybrid halide perovskite. *Nat. Energy* **1**, 16093 (2016).
73. Fu, G., Lee, D.-K., Ma, C. & Park, N.-G. Disulfidation interfacial engineering toward stable, lead-immobilizable perovskite solar cells. *ACS Energy Lett.* **8**, 4563–4571 (2023).
74. Shao, Y. et al. Grain boundary dominated ion migration in polycrystalline organic–inorganic halide perovskite films. *Energy Environ. Sci.* **9**, 1752–1759 (2016).
75. Zheng, X. et al. Defect passivation in hybrid perovskite solar cells using quaternary ammonium halide anions and cations. *Nat. Energy* **2**, 17102 (2017).
76. Feenstra, R. M. Tunneling spectroscopy of the (110) surface of direct-gap III-V semiconductors. *Phys. Rev. B* **50**, 4561–4570 (1994).
77. Beecher, A. N. et al. Direct observation of dynamic symmetry breaking above room temperature in methylammonium lead iodide perovskite. *ACS Energy Lett.* **1**, 880–887 (2016).
78. Marronnier, A. et al. Structural instabilities related to highly anharmonic phonons in halide perovskites. *J. Phys. Chem. Lett.* **8**, 2659–2665 (2017).
79. Lanigan-Atkins, T. et al. Two-dimensional overdamped fluctuations of the soft perovskite lattice in $CsPbBr_3$. *Nat. Mater.* **20**, 977–983 (2021).
80. Amat, A. et al. Cation-induced band-gap tuning in organohalide perovskites: Interplay of spin–orbit coupling and octahedra tilting. *Nano Lett.* **14**, 3608–3616 (2014).
81. Prasanna, R. et al. Band gap tuning via lattice contraction and octahedral tilting in perovskite materials for photovoltaics. *J. Am. Chem. Soc.* **139**, 11117–11124 (2017).
82. Worhatch, R. J., Kim, H., Swainson, I. P., Yonkeu, A. L. & Billinge, S. J. L. Study of local structure in selected organic–inorganic perovskites in the $Pm\bar{3}m$ phase. *Chem. Mater.* **20**, 1272–1277 (2008).
83. Laurita, G., Fabini, D. H., Stoumpos, C. C., Kanatzidis, M. G. & Seshadri, R. Chemical tuning of dynamic cation off-centering in the cubic phases of hybrid tin and lead halide perovskites. *Chem. Sci.* **8**, 5628–5635 (2017).
84. Kontos, A. G. et al. Dynamic disorder, band gap widening, and persistent near-IR photoluminescence up to at least 523 K in $ASnI_3$ perovskites (A = Cs^+, $CH_3NH_3^+$ and NH_2–CH═NH_2^+). *J. Phys. Chem. C.* **122**, 26353–26361 (2018).
85. Mukhuti, K., Sinha, S., Sinha, S. & Bansal, B. Dissipation-induced symmetry breaking: Emphanitic transitions in lead- and tin-containing chalcogenides and halide perovskites. *Appl. Phys. Lett.* **118**, 162111 (2021).
86. Zhao, X.-G., Wang, Z., Malyi, O. I. & Zunger, A. Effect of static local distortions vs. dynamic motions on the stability and band gaps of cubic oxide and halide perovskites. *Mater. Today* **49**, 107–122 (2021).
87. Gao, P. et al. Crown ether-induced supramolecular passivation and two-dimensional crystal interlayer formation in perovskite photovoltaics. *Cell Rep. Phys. Sci.* **2**, 100450 (2021).
88. Ross, R. T. Some thermodynamics of photochemical systems. *J. Chem. Phys.* **46**, 4590–4593 (2004).
89. Caprioglio, P. et al. On the relation between the open-circuit voltage and quasi-fermi level splitting in efficient perovskite solar cells. *Adv. Energy Mater.* **9**, 1901631 (2019).

90. Li, J. et al. Enhancing the efficiency and longevity of inverted perovskite solar cells with antimony-doped tin oxides. *Nat. Energy* **9**, 308–315 (2024).
91. Thiesbrummel, J. et al. Understanding and minimizing V_{OC} losses in all-perovskite tandem photovoltaics. *Adv. Energy Mater.* **13**, 2202674 (2023).
92. Al-Ashouri, A. et al. Monolithic perovskite/silicon tandem solar cell with å 29% efficiency by enhanced hole extraction. *Science* **370**, 1300–1309 (2020).
93. Savenije, T. J., Guo, D., Caselli, V. M. & Hutter, E. M. Quantifying charge-carrier mobilities and recombination rates in metal halide perovskites from time-resolved microwave photoconductivity measurements. *Adv. Energy Mater.* **10**, 1903788 (2020).
94. Hutter, E. M., Eperon, G. E., Stranks, S. D. & Savenije, T. J. Charge carriers in planar and meso-structured organic–inorganic perovskites: mobilities, lifetimes, and concentrations of trap states. *J. Phys. Chem. Lett.* **6**, 3082–3090 (2015).
95. Zhao, J., Caselli, V. M., Bus, M., Boshuizen, B. & Savenije, T. J. How deep hole traps affect the charge dynamics and collection in bare and bilayers of methylammonium lead bromide. *ACS Appl. Mater. Interfaces* **13**, 16309–16316 (2021).
96. Guo, D., Andaji Garmaroudi, Z., Abdi-Jalebi, M., Stranks, S. D. & Savenije, T. J. Reversible removal of intermixed shallow states by light soaking in multication mixed halide perovskite films. *ACS Energy Lett.* **4**, 2360–2367 (2019).
97. Hu, Y. et al. Understanding the role of cesium and rubidium additives in perovskite solar cells: trap states, charge transport, and recombination.*Adv. Energy Mater.* **8**, 1703057 (2018).
98. Hutter, E. M. et al. Charge transfer from methylammonium lead iodide perovskite to organic transport materials: efficiencies, transfer rates, and interfacial recombination. *Adv. Energy Mater.* **7**, 1602349 (2017).

Acknowledgements

M.G. acknowledges the funding from the European Union's Horizon 2020 research and innovation program GRAPHENE Flagship Core 3 under agreement No.: 881603. H.Z. acknowledges the funding support from the Shanghai Pujiang Program (22PJ1401200) and the National Natural Science Foundation of China (No. 52302229). C. Z. greatly acknowledges the Ph.D. scholarship from the China Scholarship Council (CSC, No. 202006730020). M. A. gratefully acknowledges King Abdulaziz City for Science and Technology (KACST, Saudi Arabia) for the fellowship. J.Y. acknowledges the funding support from the National Natural Science Foundation of China (No. U22A20142), the Fundamental Research Funds for the Central Universities (2023JC007), the Hebei Province Key Research and Development Project (No. 20314305D), and China Huaneng Group Co., Ltd Headquarters Science and Technology Project (HNKJ20-H88). L.E., M.A.H., and A.M. acknowledge support by SNSF grant number 200020_212046 and M.A.H. acknowledges a H2020 Marie Skłodowska-Curie Individual fellowship with grant number 101024144. A.K. acknowledges funding from the European Unions Horizon 2020 Research and Innovation program under the Marie Skłodowska-Curie Grant Agreement No. 843453. A.R. and T.G. acknowledge funding from the Fonds National de la recherche, project number: Nr. 11244141. The authors acknowledge Dr. Anwar Alanazi's help with device optimization.

Author contributions

M.G. and H.Z. supervised the study. H.Z. and Z.Z. conceived the idea and designed the experiments. H.Z., Z.Z., C.Z., and M.A. conducted the device fabrication and characterization. H.Z., M.G., Z.Z., and J.Y. have conceptually contributed to the project while being involved in the mechanistic investigation, analysis, as well as project coordination. Z.Z., M.A., and C.Z. participated in device optimization and assisted in some sample preparations. F.E., M.A., and Z.Z. performed the PLQY characterizations and the analysis of the optoelectronic loss mechanisms. C.Z., H.Z., and J.X. performed the Suns-PLQY and Suns-QFLS measurements and analysis of the FF loss. A.M., M.A.H., and L.E. performed the solid-state NMR studies and analysis. C.Z. performed the SEM, XRD, and GIXRD. J.Z. and T.J.S performed the TRMC characterization. Z.Z. and M.A. prepared the samples for AFM characterization, and A.R. and T.G. performed the AFM and KPFM characterization. H.Z., A.K., C.Z., M.A., and Z.Z. assisted in device stability tests and data analysis. S.M.Z., Y.Y., J.X., and J.Y. were involved in discussion and project coordination. H.Z. and C.Z. wrote the first manuscript draft, and all the authors contributed to the revision.

Competing interests

The authors declare no competing interests.

Additional information

Supplementary information The online version contains supplementary material available at https://doi.org/10.1038/s41467-024-51550-z.

Correspondence and requests for materials should be addressed to Zhiwen Zhou, Jianxi Yao, Hong Zhang or Michael Grätzel.

Peer review information *Nature Communications* thanks Antonio Abate, Changduk Yang, and the other anonymous, reviewer(s) for their contribution to the peer review of this work. A peer review file is available.